O$_2$($^1\Delta$) production in flowing He/O$_2$ plasmas. I. Axial transport and pulsed power formats

D. Shane Stafford[a)]
Department of Theoretical and Applied Mechanics, University of Illinois, Urbana, Illinois 61801

Mark J. Kushner[b)]
Department of Electrical and Computer Engineering, Iowa State University, Ames, Iowa 50011

Chemical oxygen-iodine lasers (COILs) have promising applications due to their high efficiency and ease of scaling to multikilowatt powers. Recent research has focused on pumping the iodine with O$_2$($^1\Delta$) produced by electric discharges. In a previous work, a global model was used to develop reaction mechanisms and determine the specific energy deposition (eV/O$_2$) required to obtain high O$_2$($^1\Delta$) yields for electric discharge COILs. Experiments have recently achieved positive laser gain and oscillation with these energy depositions and have highlighted the importance of axial expansion of the plasma in optimizing excitation of the O$_2$($^1\Delta$). In this work, the consequences of axial transport on O$_2$($^1\Delta$) yields have been computationally investigated in flowing He/O$_2$ plasmas at a few Torrs using a one-dimensional plasma hydrodynamics and kinetics model. We show that the experimentally observed extension of the plasma glow upstream and downstream of the electrodes is due to electron diffusion and capacitive coupling of the radio-frequency power source. We also show that $\approx$50% higher O$_2$($^1\Delta$) yields can be achieved with a pulsed discharge combined with continuous-wave discharge. © *2005 American Institute of Physics.* [DOI: 10.1063/1.2076427]

I. INTRODUCTION

The coherent infrared light available from chemical oxygen-iodine lasers (COILs) couples efficiently with most metals and is easily transmitted through fiber optics. The COIL is also highly efficient and capable of scaling to multikilowatt continuous-wave (cw) power, making it attractive for diverse applications.[1–7] COILs obtain the 1.315 μm beam by pumping I$_2$ with the O$_2$($^1\Delta$) metastable energy donor which first dissociates the I$_2$ into atomic I. Further collisions with O$_2$($^1\Delta$) excite the atomic I to the upper laser level, creating a population inversion and subsequent lasing on the $^2P_{1/2} \rightarrow {}^2P_{3/2}$ magnetic dipole transition. Conventional COILs efficiently produce O$_2$($^1\Delta$) via caustic liquid-phase chemistry, achieving yields up to 0.7.[8] However, because of the inherent hazards, complexity, and overall weight of the liquid-phase system, recent experimental efforts have focused on developing all-gas-phase O$_2$($^1\Delta$) generators.[9,10]

In many of the current all-gas-phase experiments, the O$_2$($^1\Delta$) metastable is generated via flowing electric discharges in pure O$_2$ or in mixtures with inert gases such as N$_2$ and He. These experiments involve capacitive, inductive, or microwave self-sustained electric discharges or e-beam non-self-sustained discharges.[2,11–15] The threshold O$_2$($^1\Delta$) yield required for positive laser gain for conventional systems can be derived by assuming that the forward and reverse rates of the pumping reaction are at equilibrium,[16]

$$Y = \frac{1}{1 + 1.5e^{401/T}},\tag{1}$$

where the cavity temperature T is in units of Kelvin. At room temperature the threshold yield is 0.15.

Early attempts to produce O$_2$($^1\Delta$) in self-sustained electric discharges resulted in relatively low yields of 0.11–0.14.[17,18] More recent investigations have reported yields over 0.15 by engineering the reduced electric field (E/N) nearer to the optimum value for O$_2$($^1\Delta$) production using non-self-sustained configurations such as pulsed avalanche discharges[11] and e-beam-sustained discharges.[15] Various additives (e.g., H$_2$, D$_2$, CO, NO, or NO$_2$) have been investigated for use in tailoring the E/N to lower, more favorable values through a reduction in the overall ionization potential of the gas mixture.[13,15,19] Moderate yields at higher pressures have also been obtained through the addition of inert diluents (e.g., Ar and He) and unconventional discharge geometries.[20,21]

In a previous work, we presented results from a computational investigation of O$_2$($^1\Delta$) yields produced by self-sustained discharges in He/O$_2$ mixtures using a global plasma kinetics model.[22] We showed that yields of O$_2$($^1\Delta$) scale linearly with O$_2$ specific energy deposition for typical COIL discharges, where O$_2$($^1\Delta$) yield is defined as

$$Y = \frac{[O_2(^1\Delta)]}{[O_2 \text{ equivalent species}]},\tag{2}$$

and specific energy deposition is

a)Electronic mail: dstaffor@uiuc.edu
b)Author to whom correspondence should be addressed; electronic mail: mjk@iastate.edu

98, 073303-1

$$\bar{E}_d = \frac{E_d}{[\text{O}_2 \text{ equivalent species}]}, \tag{3}$$

where [O_2 equivalent species] denotes the sum of the densities of all oxygen-containing species on a molecular O_2 basis, and E_d is the volumetric specific energy deposition (eV/cm^3). Peak $\text{O}_2(^1\Delta)$ yields were obtained with $\bar{E}_d \approx 5$ eV/molecule of O_2 equivalent species. For $\bar{E}_d > 5$ eV, the O_2 was mostly dissociated causing $\text{O}_2(^1\Delta)$ yields to decrease. We also showed that when $\bar{E}_d$ is held constant, moderate variations in composition, power deposition, and pressure produce much smaller, secondary effects in $\text{O}_2(^1\Delta)$ yield than changes in $\bar{E}_d$. Furthermore, these secondary effects were shown to be even less important in the context of the combined yield of $\text{O}_2(^1\Delta)$ and $\text{O}_2(^1\Sigma)$. The secondary effects were shown to influence the $\text{O}_2(^1\Sigma)/\text{O}_2(^1\Delta)$ ratio, but they have a small influence on the ultimate $\text{O}_2(^1\Delta)$ yield far downstream of the discharge due to the rapid quenching of $\text{O}_2(^1\Sigma)$ to $\text{O}_2(^1\Delta)$ by collisions with O atoms. These results were validated with experiments, and a complete kinetic rate sensitivity analysis showed that the global model results were robust to moderate uncertainties in the rate coefficient data.

Using specific energy deposition in the range suggested by the global model, Carroll *et al.* have recently reported positive gain and oscillation in an electric discharge-pumped COIL.[23,24] Their configuration uses a capacitive coupled discharge in He and O_2 at moderate power levels and pressures. In order to reduce the operating E/N of the gas, NO was added at the inlet. NO_2 was also injected downstream of the discharge to scavenge O atoms before the iodine injection point to eliminate detrimental quenching of I*. Measurements of excited-state densities with this configuration revealed the upstream and downstream penetrations of the plasma beyond the electrodes and highlighted the importance of axial transport in the plasma.[14] Photographs by Rakhimova *et al.* of the glow region in a transverse discharge in flowing air also show propagation of the glow past the ends of the external electrodes in both the upstream and downstream directions.[20] This evidence of strong axial transport effects in addition to recent progress with pulsed discharges in O_2, such as that by Hicks *et al.*, illustrates the need for a more capable numerical plasma hydrodynamics model.[25]

In this work, a one-dimensional (1D) axially flowing plasma kinetics model was developed to investigate the consequences of axial transport of mass, momentum, and energy on the $\text{O}_2(^1\Delta)$ yield, with specific focus on elongation of the discharge area. In addition, a pulsed discharge model was developed to investigate the pulsed-sustainer avalanche discharge proposed by Hill.[11] We found that although the axial transport tends to elongate the plasma glow region, the energy scaling law derived using the global model is still valid for cw discharges including axial flow in spite of the extension of the plasma upstream and downstream of the electrodes. The inclusion of axial transport tended to reduce the average electron temperature in the discharge region, raising the $\text{O}_2(^1\Delta)$ yield (favored by lower electron temperatures). Spiker-sustainer discharges were found to significantly im-
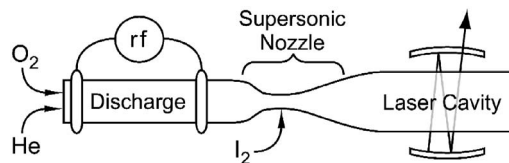

FIG. 1. Schematic of typical electric discharge COIL. O_2 is mixed with an inert gas and flowed through the discharge. The gases are then cooled by supersonic expansion before entering the laser cavity.

prove $\text{O}_2(^1\Delta)$ yield beyond that predicted by the $\bar{E}_d$ scaling, showing great promise for future electric discharge COIL experiments.

A description of the axial transport algorithms is in Sec. II. The reaction mechanism is reviewed in Sec. III. Results from the simulations and a discussion of the consequences of pulsing are discussed in Secs. IV and V. Concluding remarks are in Sec. VI.

II. DESCRIPTION OF THE MODEL

A schematic of a typical electrical discharge COIL device is shown in Fig. 1. Oxygen and a diluent such as He are first fed through a quartz tube, where the plasma is sustained by an electric discharge. Additives such as H_2, CO, or NO may also be used usually to increase the net rate of ionization,[15,23] but will not be discussed here. Powers of tens to hundreds of watts are deposited into gases flowing at hundreds to thousands of cm/s. Pressures are a few to tens of Torrs for O_2 mixtures with mole fractions of 0.03–1 with the balance being the inert gas diluent. The gases may be precooled before entering the discharge but usually enter at about 300 K. The discharge section is usually a few tens of centimeter in length and a few centimeters in diameter. Following the plasma, the excited oxygen and diluent are fed through a nozzle where I_2 is injected into the flow. To aid in mixing the I_2 secondary flow is typically injected tangentially to the primary flow in the subsonic portion of a supersonic nozzle. The gases then mix, react, and cool as they flow through the transonic and supersonic portions of the nozzle. Ideally the gases are cooled to around 140 K as they flow through the laser cavity and are drawn into the exhaust system.[19]

GlobalKin, a global plasma kinetics model,[22] was modified to include 1D axial transport for this computational investigation. GlobalKin consists of three main modules which address gas-phase chemistry and transport, solution of Boltzmann's equation for the electron energy distribution (EED), and a module for integration of the partial—and ordinary-partial differential equations that result. The reaction chemistry and transport module construct differential equations for the time evolution of species densities and temperatures using the results obtained from the solution of Boltzmann's equation which provides electron-impact rate coefficients. The stiff ordinary differential equation (ODE) solver then integrates the system of differential equations.

In addition to the global plasma kinetics model discussed in Ref. 22, the one-dimensional model constructs equations

for axial flux of mass, momentum, gas energy, and electron energy. Total mass conservation and species evolutions (charged and neutral) are described by

$$\frac{\partial \rho}{\partial t} + \nabla \cdot (\rho \boldsymbol{\nu}) = 0, \tag{4}$$

$$\frac{\partial N_i}{\partial t} = -\nabla \cdot [N_i(\boldsymbol{\nu} + \boldsymbol{\nu}_{\text{diff},i} + \boldsymbol{\nu}_{\text{drift},i})] + S_i + W_i, \tag{5}$$

where ρ is the total mass density and N_i is the density of species i. Axial transport occurs through the combination of the bulk advective velocity $\boldsymbol{\nu}$, and the diffusive and drift velocities of component i, $\boldsymbol{\nu}_{\text{diff},i}$ and $\boldsymbol{\nu}_{\text{drift},i}$. The reaction sources S_i and radial fluxes W_i are the same as in the global model. The diffusion and drift velocities are obtained from the diffusivities D_i and mobilities μ_i,

$$\boldsymbol{\nu}_{\text{diff},i} = -\frac{1}{x_i} D_i \nabla x_i, \tag{6}$$

$$\boldsymbol{\nu}_{\text{drift},i} = q_i \mu_i \mathbf{E}_a, \tag{7}$$

where x_i is the mole fraction, q_i is the charge, and μ_i is the mobility of species i. The axial electric field $\mathbf{E}_a$ was obtained by assuming an ambipolar field, whereby the axial charged fluxes are assumed to sum to zero at any axial point in the discharge. The ambipolar field can then be calculated at any point by

$$\mathbf{E}_a = -\frac{\sum_i q_i N_i(\boldsymbol{\nu} + \boldsymbol{\nu}_{\text{diff},i})}{\sum_i q_i^2 \mu_i N_i}. \tag{8}$$

An upwind discretization was utilized for the heavy particle advective flux and drift flux terms to preserve their hyperbolic character and provide some robustness against numerical instabilities. Since the ambipolar field assumption requires a net zero charge flux at any point, the electron density must always equal the net heavy particle charge density for neutral initial conditions and the electron density need not be calculated explicitly via Eq. (5).

To obtain the axial gas advective speed, the momentum continuity equation for cylindrical geometry [Eq. (9)] may be integrated,

$$\frac{\partial (\rho \boldsymbol{\nu})}{\partial t} + \nabla \cdot (\rho \boldsymbol{\nu}\boldsymbol{\nu} + p + \boldsymbol{\tau}) = 0, \tag{9}$$

$$\nabla \cdot \boldsymbol{\tau}_z = \frac{\partial \tau_{zz}}{\partial z} + \frac{4\mu \nu_{\text{max}}}{R^2}, \tag{10}$$

$$\tau_{zz} = -\frac{4}{3}\mu \frac{\partial \nu_z}{\partial z}, \tag{11}$$

where ρ is the mass density, $\boldsymbol{\nu}$ is the axial velocity, p is the thermodynamic pressure, and μ is the mixture-averaged viscosity. The divergence of the stress tensor $\boldsymbol{\tau}$ is evaluated in the axial direction assuming laminar flow with no-slip boundary conditions at the wall, as represented by Eqs. (10) and (11). The maximum velocity at the center of the discharge ν_{max} is obtained from the specified flow conditions

and the resulting parabolic axial velocity profile. For typical low Mach number discharges at around 300 K, the pressure variations predicted by Eq. (9) will be small compared to the total pressure. If, ultimately, only steady-state conditions are desired, then to save computational time the pressure can be fixed, and the velocity can then be calculated assuming a constant axial mass flux. In either case, the relationship between pressure, density, and temperature is given by the ideal-gas equation of state

$$p = f(N, T_g) = N k_B T_g, \tag{12}$$

where T_s is the gas temperature and k_B is Boltzmann's constant.

The gas temperature is obtained while considering contributions from the upwinded axial advection and conduction, viscous dissipation, p-V work, radial conduction, reaction sources, and elastic electron impact,

$$\rho c_P \frac{\partial T_{\text{gas}}}{\partial t} = -\rho \boldsymbol{\nu} c_P \cdot \nabla T_{\text{gas}} - \nabla \cdot \mathbf{q} - \tau_{zz} \nabla \cdot \boldsymbol{\nu} + \frac{Dp}{Dt}$$
$$+ \frac{\kappa}{\Lambda^2}(T_{\text{wall}} - T_{\text{gas}}) + \Delta h_{\text{rxn}} + h_e, \tag{13}$$

$$\mathbf{q} = -\kappa \nabla T_{\text{gas}}, \tag{14}$$

$$\Delta h_{\text{rxn}} = \sum_j \Delta h_j^\circ k_j \prod_l N_l^{a_{lj}^{(\text{LHS})}}, \tag{15}$$

$$h_e = \sum_i \frac{3}{2} n_e \nu_{mi} \left(\frac{2m_e}{M_i}\right) k_B (T_e - T_{\text{gas}}). \tag{16}$$

The heat capacity c_P and thermal conductivity κ are mixture averaged, and the radial conduction term is estimated using the diffusion length Λ. The conduction flux $\mathbf{q}$ and heat of reaction Δh_{rxn} are defined by Eqs. (14) and (15), where Δh_j° and k_j are the heat and rate coefficients of the jth reaction, and $a_{lj}^{(\text{LHS})}$ is the stoichiometric coefficient of reactant l in the jth reaction. These processes also include Frank-Condon heating from electron-impact dissociation of molecules. Elastic heating from electron momentum transfer collisions h_e is given by Eq. (16), where ν_{mi} and M_i are the collision frequency and mass of component i, and n_e and m_e are the electron density and mass, respectively. If the momentum equation is not integrated (fixed mass flux), then the viscous dissipation and p-V work terms are assumed to be small and are thus neglected.

The electron temperature is obtained by considering contributions from axial electron flux, joule heating, and elastic and inelastic impacts with heavy neutrals and ions,

$$\frac{\partial \left(\frac{3}{2} n_e k_B T_e\right)}{\partial t} = -\nabla \cdot \mathbf{q}_e + P_d - h_e + \sum_l n_e k_l N_l \Delta \varepsilon_l, \tag{17}$$

$$\mathbf{q}_e = \frac{5}{2} \boldsymbol{\Gamma}_e k_B T_e - \lambda_e \nabla k_B T_e, \tag{18}$$

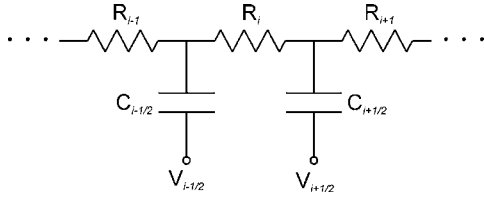$$\boldsymbol{\Gamma}_e = \mu_e q_e n_e \mathbf{E} - D_e \nabla n_e, \tag{19}$$

FIG. 2. Schematic of transmission line discharge model. Each computational mesh cell has an associated plasma resistance R_i, and each midpoint has an associated capacitance $C_{i\pm1/2}$, to the drive voltage $V_{i\pm1/2}$. The drive voltage is set to zero (ground) except at the driven electrode.

$$\lambda_e = \frac{5}{2}\frac{n_e k_B T_e}{m_e \nu_{m,\mathrm{av}}}, \tag{20}$$

$$D_e = \frac{k_B T_e}{m_e \nu_{m,\mathrm{av}}}, \tag{21}$$

where P_d is the volumetric power deposition (Joule heating), and $\Delta\varepsilon_l$ is the electron energy gain from the lth electron-impact reaction. The electron heat flux $\mathbf{q}_e$ is given by Eq. (18) and consists of terms accounting for electron flux and conduction, where $\boldsymbol{\Gamma}_e$ is the axial flux given in Eq. (19) and λ_e is the electron thermal conductivity given by Eq. (20). The flux $\boldsymbol{\Gamma}_e$ consists of drift and diffusion, where μ_e is the electron mobility, q_e is the electron charge, $\mathbf{E}$ is the axial ambipolar electric field, and D_e is the electron diffusivity given by Eq. (21). The electron thermal conductivity λ_e and diffusivity D_e are functions of the average electron-impact momentum-transfer collision frequency $\nu_{m,\mathrm{av}}$. An upwind discretization was used for the drift portion of the electron flux.

The electron-transport coefficients used in Eqs. (17)–(21) are calculated by solving Boltzmann's equation for the EED.[22,26] Since the species mole fractions vary significantly both spatially and temporally, the EED and electron-impact rates are strong functions of position and time. Since it would be computationally expensive to evaluate the Boltzmann equation at each grid location for every time step, an approximation is necessary. Therefore, in the one-dimensional scheme the Boltzmann solver calculates the electron-transport coefficients as a function of position only. Then, at various time intervals on the approach to the steady solution, the Boltzmann solver is called to update the coefficients at each position along the axis. With the judicious choice of a few update intervals, the time taken for convergence to steady state is only slightly increased.

For the power deposition model we assumed purely capacitive coupling. In this model, a transmission line approach was utilized, where each mesh cell in the discretization is represented by its associated plasma resistance R_i, as shown in Fig. 2. A capacitance $C_{i\pm1/2}$ is attached at each midpoint and is driven by a sinusoidal voltage $V_{i\pm1/2}$, where the capacitance is represented by its complex reactance $-j/\omega C_{i\pm1/2}$, and the voltage is the root mean square of the sinusoidal driving voltage. The capacitances are estimated based on the geometry of the companion experiments. The transmission line model facilitates the simulation of any number and length of internal or external electrodes. Except for the driven electrode, all of the voltages $V_{i\pm1/2}$ are set to zero (ground). The voltages and currents at each midpoint

are described using Ohm's and Kirchoff's laws and the resulting tridiagonal complex system of equations is implicitly solved. The power depositions are then found by

$$P_{d,i} = \Re\left(\frac{V_{R,i} V_{R,i}^*}{R_i}\right), \tag{22}$$

where $V_{R,i}$ is the complex voltage drop across the plasma resistance R_i at the ith grid point.

Using the capacitively coupled plasma (CCP) model, power may be pulsed using a variable duty cycle wave form. The pulse period, pulse width, rise, and fall times are specified. The average power is then scaled by the specified wave form as a function of time. A background power level may also be specified, whereby an avalanche-sustained discharge of the type described by Hill may be simulated.[11]

The one-dimensional system of equations is discretized on a mesh having variable spacing producing a system of ODEs. Dirichlet boundary conditions are prescribed for the inlet of the discharge; von Neumann boundary conditions are prescribed at the outlet. When the momentum equation [Eq. (9)] is solved, a Dirichlet boundary condition is specified at the outlet to hasten convergence to a steady-state solution. A double precision variable-coefficient ODE solver developed at LLNL as part of ODEPACK was used with the method of lines to obtain the time-dependent one-dimensional solution.[27]

III. REACTION MECHANISM

The reaction mechanism used in this investigation involves reactions in the gas-phase discharge and afterglow as well as recombination and quenching reactions on the discharge tube walls. The species in the mechanism include ground-state neutrals O_2, O, O_3, and He; vibrational and electronic states $O_2(v)$, $O_2(a\,^1\Delta)$, $O_2(b\,^1\Sigma)$, $O(^1D)$, and $O(^1S)$; and ions O_2^+, O^+, O_2^-, O^-, and O_3^-. [$O_2(v)$ represents the total vibrational population consisting of the first four vibrational levels of O_2.] The $He(^2S)$ and He^+ states were included in the investigation using the global kinetics model; however, they were occasionally not included in the 1D model because their maximum densities were found to be less than 10^3 and the computations proceed somewhat faster without including them. The complete gas phase and wall reaction mechanism is discussed in detail in Ref. 22 and is briefly outlined below.
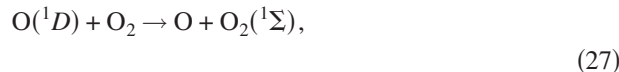
Electron-impact reactions dominate the kinetics in the discharge region. At the discharge inlet, where only ground-state O_2 and He are present, the O_2 is excited to electronic states and dissociated by electron-impact reactions,
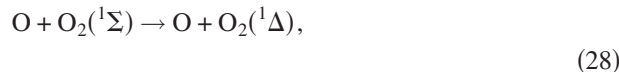
$$e + O_2 \rightarrow O_2(^1\Delta + e, \tag{23}$$

$$e + O_2 \rightarrow O_2(^1\Sigma) + e, \tag{24}$$

$$e + O_2 \rightarrow O + O + e. \tag{25}$$

Further along in the discharge when the dissociated fraction becomes significant, electron-impact excitation of O atoms gives $O(^1D)$,

$$e + O \rightarrow O(^1D) + e. \tag{26}$$
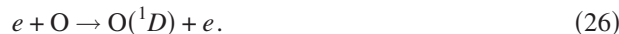
$O(^1D)$ then contributes to $O_2(^1\Delta)$ production through a sequence of collisions with O_2,

$$O(^1D) + O_2 \rightarrow O + O_2(^1\Sigma),$$

$$k = 2.0 \times 10^{-11} \text{ cm}^3 \text{ s}^{-1} \text{ (Ref. 28)}, \tag{27}$$

$$O + O_2(^1\Sigma) \rightarrow O + O_2(^1\Delta),$$

$$k = 7.2 \times 10^{-14} \text{ cm}^3 \text{ s}^{-1} \text{ (Ref. 28)}, \tag{28}$$

where k is the rate coefficient at 300 K.

As the $O_2(^1\Delta)$ density increases in the downstream portion of the discharge, the $O_2(^1\Delta)$ production processes must compete with $O_2(^1\Delta)$ losses to upper electronic states, dissociation, and superelastic deexcitation to the ground state,

$$e + O_2(^1\Delta) \rightarrow O_2(^1\Sigma) + e, \tag{29}$$

$$e + O_2(^1\Delta) \rightarrow O + O + e, \tag{30}$$

$$e + O_2(^1\Delta) \rightarrow O_2 + e. \tag{31}$$

In this downstream region the discharge becomes less efficient at producing $O_2(^1\Delta)$, and atomic O is produced instead.

At the end of the discharge region, the remaining $O_2(^1\Sigma)$ is quickly quenched to $O_2(^1\Delta)$ by collisions with O atoms [Eq. (33)]. The $O_2(^1\Delta)$ then persists far into the afterglow due to its 64.4 min radiative lifetime,[29] where the most significant quenching mechanism is through collisions with O atoms,

$$O_2(^1\Delta) + O \rightarrow O_2 + O,$$

$$k = 2.0 \times 10^{-16} \text{ cm}^3 \text{ s}^{-1} \text{ (Ref. 30)}. \tag{32}$$

A simple wall reaction mechanism describes the species diffusing to and returning from the walls. In this mechanism, all ions are neutralized at the wall and return as ground-state species. Two percent of the $O_2(^1\Sigma)$ is quenched to the ground state, and 2% of the atomic O reaching the wall recombines to form ground-state O_2. The rate of $O_2(^1\Delta)$ quenching by the wall is insignificant at typical COIL conditions, occurring with a probability of 10^{-5} on Pyrex.[31]

IV. AXIAL TRANSPORT IN HE/O$_2$($^1\Delta$) PLASMAS

The base case uses conditions similar to experiments performed by Carroll *et al.*, which achieved positive gain in an electric discharge COIL system.[23] The gases flow through a 4.8-cm-i.d. Pyrex discharge tube, with capacitive electrodes on the discharge tube outer diameter spaced 20 cm apart. The driven electrode is upstream of the ground electrode. The total pressure is 10.6 Torr, with a He/O$_2$=80/20 mixture is fed into the discharge at 20 mmol/s. This flow rate corresponds to an axial velocity of ≈ 2000 cm/s into the discharge region. The absorbed power in the base case is 340 W at 13.56 MHz. The capacitances required for the CCP transmission line parameters (Fig. 2) were calculated based on geometry, assuming an infinitely long coaxial capacitor
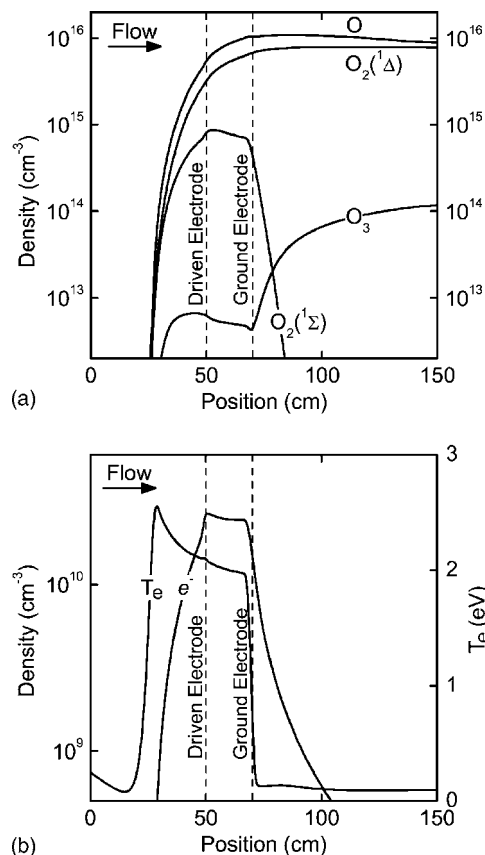

FIG. 3. Plasma properties for the steady-state base case for an inlet flow of 20 mmol/s He/O$_2$=80/20 at 10.6 Torr and 300 K. The CCP discharge is 340 W at 13.56 MHz with the driven electrode at 50 cm, ground electrode at 70 cm. (a) O$_2$($^1\Delta$), O$_2$($^1\Sigma$), O atom, and O$_3$ densities. (b) Electron density and temperature.

(the discharge tube) suspended above a 15-cm-wide ground plane 15 cm below the discharge tube. This configuration in conjunction with the geometry and material properties of the Pyrex discharge tube yields capacitances on the order of 100 pF/cm. The capacitance at the external electrodes is larger by a factor of 100.

Densities of O$_2$($^1\Delta$), O$_2$($^1\Sigma$), O, and O$_3$ for the base case are shown in Fig. 3(a). The axial length of the computational domain is 150 cm, with the upstream (driven) electrode being 50 cm from the inlet, and the downstream (ground) electrode being 70 cm from the inlet. The results shown in Fig. 3 correspond to the steady state. (Although the one-dimensional model is time dynamic, only steady-state results will be discussed here.) Comparing these results to those of the base case for the global kinetics model (see Ref. 22), we see that the species densities at the end of the discharge region are roughly the same for both cases. The O atom density exceeds the O$_2$($^1\Delta$) density, and the O$_2$($^1\Sigma$) density decreases rapidly in the afterglow. In addition, O$_3$ does not begin to play an important role until the afterglow, several tens of centimeter downstream of the discharge region. However, we see that the most significant difference between the global and one-dimensional models is that the species densities in Fig. 3(a) begin to increase far upstream (≈ 20 cm) of the driven electrode. This is partly due to the axial transport of the plasma and partly due to an extended region of power deposition resulting from the capacitive coupling.

The extent of the plasma zone is shown more clearly in the profile of the electron density in Fig. 3(b). The electron density reaches 10^9 cm^{-3} by 20 cm upstream of the driven electrode because of upstream transport (diffusion) of electrons and subsequent ionization. The steep rise in electron density at this point marks the front end of the reactive plasma zone. Power deposition becomes important at this position, and electron-impact processes with O_2 begin to dominate the kinetics. The electron temperature spikes upstream of this point due, in part, to the large fringing electric fields and low conductivity which initiate an avalanche process. The spike in T_e is not as large as with the global model because of there being axial transport of electrons upstream of the main plasma zone which produces a non-negligible conductivity, thereby facilitating power deposition by capacitive coupling. The same action occurs on the downstream side of the discharge, increasing the length of the afterglow. The asymmetry of the electron density is due in part to downstream advection and in part to dissociation of the O_2 that produces a more readily ionized gas mixture.

The consequences of increasing the power while maintaining other conditions are shown in Fig. 4. The average electron density in the bulk plasma zone increases roughly linearly with power deposition, as shown in Fig. 4(a). The plasma zone extends further upstream and downstream of the electrodes as the power is increased, an effect facilitated by a higher axial conductivity enabling the capacitive coupling to reach further away from the region between the electrodes.

When the input powers are converted to specific energy depositions, the peak $O_2(^1\Delta)$ yield generally scales with specific energy deposition, as shown in Fig. 4(b). These results closely parallel those obtained with the global model for peak $O_2(^1\Delta)$ yields, albeit over a smaller parameter space, of up to 3 eV/molecule deposited into O_2 equivalent species. The peak gas temperature also increases rapidly with specific energy deposition, reaching almost 800 K by 3 eV/molecule. The O atom density as a function of specific energy deposition, shown in Fig. 4(c), increases at a higher rate than the $O_2(^1\Delta)$ density as specific energy deposition is increased due to contributions from dissociative attachment. These results are also similar to those from global model. Therefore, to first order, the scaling $O_2(^1\Delta)$ production proposed based on the results from the global plasma kinetic modeling, discussed in Ref. 22, also appear to hold when axial transport and capacitive power deposition are also considered.

The effect of increasing the inlet flow rate is shown in Fig. 5. The power has also been increased to compensate for the reduced residence time of gases in the plasma zone so that the overall specific energy deposition remains approximately constant. As the power increases the electron density increases by roughly the same factor, as shown in Fig. 5(a). With increasing flow rate, the afterglow region extends further downstream. Although the expansion of the plasma zone can be partially attributed to the increase in power, there is an additional flow-induced expansion of the plasma zone [compare Fig. 5(a) to Fig. 4(a)]. This extension results from the residence time of the gas in the plasma zone being shorter or commensurate to the time for recombination and
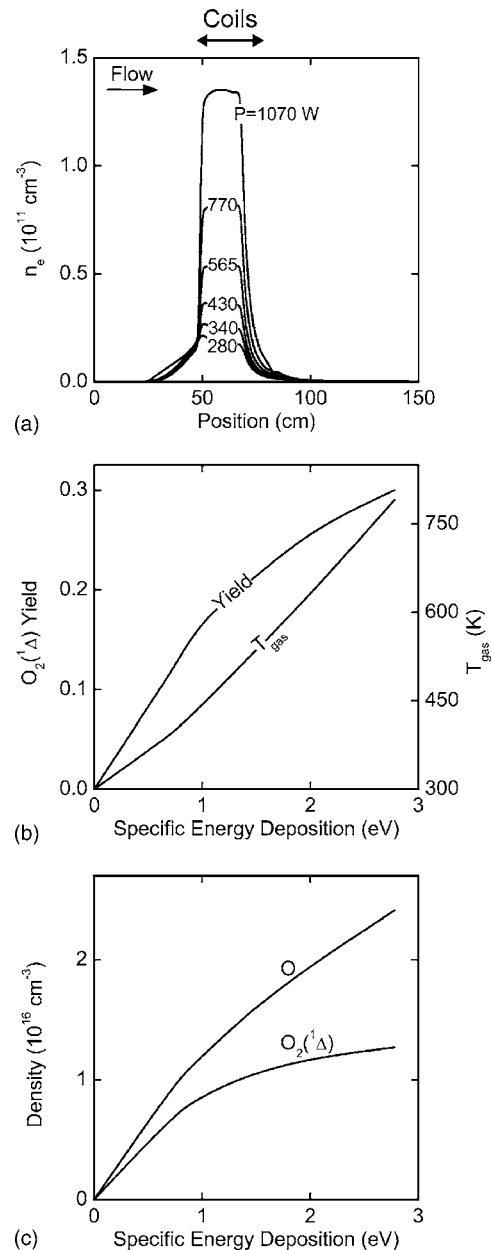

FIG. 4. Consequences of power deposition on plasma properties. Conditions are otherwise the same as for the base case. (a) Electron densities at various powers as a function of distance along the axis. (b) Peak $O_2(^1\Delta)$ yield and T_g where power has been converted to specific energy deposition. (c) Peak $O_2(^1\Delta)$ and O atom densities as a function of specific energy deposition. As with the zero-dimensional (0D) model, $O_2(^1\Delta)$ yield scales with specific energy deposition at these conditions.

diffusion to extinguish the plasma. As the residence time decreases with increasing flow rate while the quenching time remains nearly constant, the plasma extends downstream. Had the quenching time for the plasma been very short compared to the residence time, the increased flow rate would not have extended the plasma downstream. The increased extension of the plasma facilitated by the flow has a little effect on the electron temperature, as shown in Fig. 5(b). Consequently, the electron-impact reaction-rate coefficients do not change significantly. Although the location of the peak $O_2(^1\Delta)$ yield is shifted downstream by the increasing veloc-
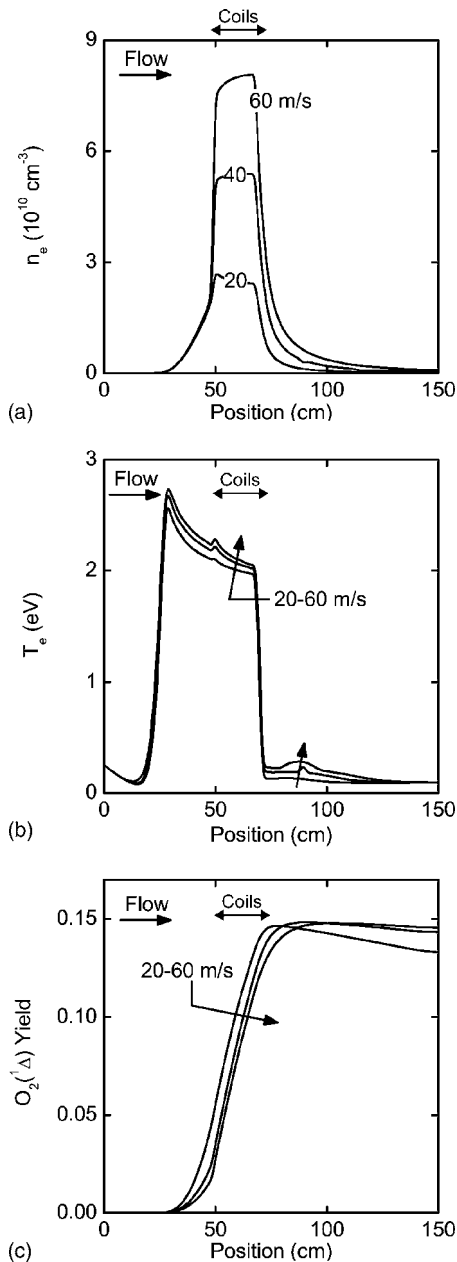
(a)

(b)

(c)

FIG. 5. Consequences of gas flow rate. The inlet flow rate was increased from 20 mmol/s (base case) to 40 and 60 mmol/s, which correspond to ≈ 20, 40, and 60 m/s inlet speeds. Power was increased from 340 W (base) to 680 and 1020 W to keep $\bar{E}_d$ constant. Other conditions are the same as for the base case. (a) Electron density and (b) temperature as a function of distance along the discharge tube axis. (c) $O_2(^1\Delta)$ yield along the discharge. The increasing flow velocity causes the location of peak $O_2(^1\Delta)$ yield to move further down the discharge tube, but the value of the peak $O_2(^1\Delta)$ yield does not change.
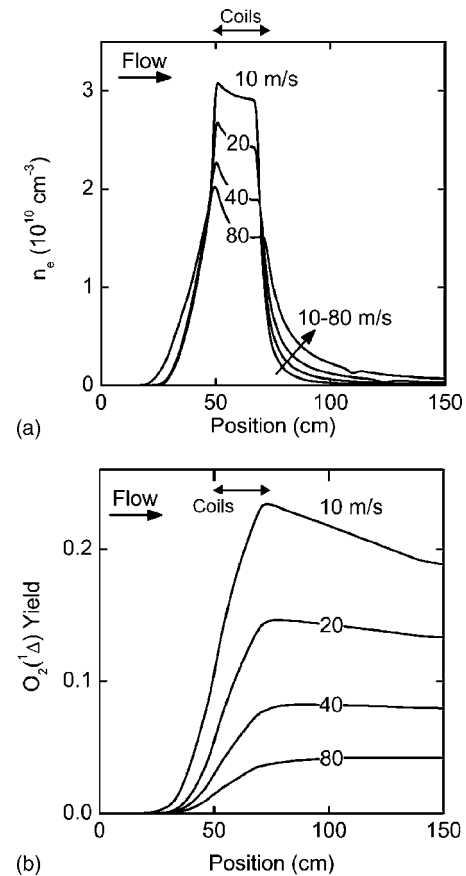

(a)

(b)

FIG. 6. Plasma properties while varying inlet flow speeds. The results are shown for flow rates of 10, 20, 40, and 80 mmol/s, which correspond to ≈ 10, 20, 40, and 80 m/s inlet speeds. Other conditions, including power, are the same as for the base case (Fig. 3). (a) Electron density and (b) $O_2(^1\Delta)$ yield along the discharge. The increasing flow velocity causes expansion of the downstream portion of the plasma zone due to momentum transfer from the bulk fluid to the ions. $O_2(^1\Delta)$ decreases with flow rate as power is kept constant and specific energy deposition decreases.

ity, the absolute value is close to the base case value [Fig. 5(c)] since the specific energy deposition has been held constant.

The flow-induced expansion of the plasma is readily apparent when the power is kept constant while the inlet velocity is increased, as shown in Fig. 6(a), which reduces the specific energy deposition. Here, the bulk electron density in the discharge decreases approximately linearly with specific power deposition. However, even though the bulk electron density decreases with increasing flow, the plasma zone is

further extended with larger inlet speeds so that the electron density increases tens of centimeter downstream of the electrodes. This flow-induced expansion of the plasma is due to momentum transfer from the bulk fluid to the ions. As the flow rate increases and residence time in the plasma decreases, the specific energy deposition also decreases. As such, there is less dissociation and less excitation, resulting in a more attaching gas mixture (lower electron density) and lower $O_2(^1\Delta)$ yield, as shown in Fig. 6(b).

Based on the investigations with the global model, the addition of He diluent was shown to have a small effect on $O_2(^1\Delta)$ yields. In particular, the addition of He was shown to increase the $[O_2(^1\Delta)]/[O_2(^1\Sigma)]$ ratio in the discharge, while only weakly affecting the total $O_2(^1\Delta)+O_2(^1\Sigma)$ density. He addition also had a weak influence on yields when considering axial flow, with the net effect being that the $O_2(^1\Delta)$ yield decreases as He is added, as shown in Fig. 7(a). The large thermal conductivity of He/O_2 mixtures also results in similar gas temperatures for the various mixtures 1 m downstream of the discharge [Fig. 7(b)]. The addition of He also has a small effect on the efficiency of $O_2(^1\Delta)$ production, where efficiency is defined as $[O_2(^1\Delta)\text{yield}]/[\bar{E}_d]$. When the He mole fraction is increased from 50% to 85%, the effi-
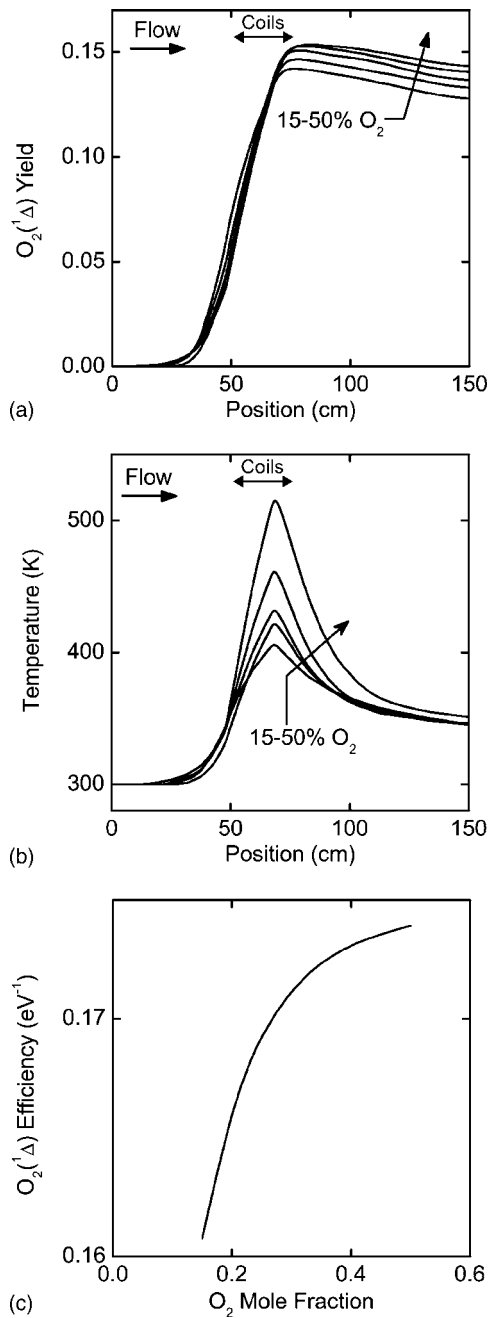
FIG. 7. Plasma properties for dilution of the O_2 flow with He. Conditions are the same as in Fig. 3 with the O_2 molar flow and partial pressure held constant as He is added to the flow. (a) $O_2(^1\Delta)$ yield along the discharge for 15%, 20%, 25%, 35%, and 50% O_2 mixtures in He. (b) Gas temperature. (c) Efficiency of $O_2(^1\Delta)$ production. The addition of He reduces T_g, but decreases the efficiency of $O_2(^1\Delta)$ production for these conditions.

ciency of $O_2(^1\Delta)$ production changes by only a few percent, as shown in Fig. 7(c). Therefore, as predicted by the global model, the effect of He addition is much weaker than the first-order scaling with $\bar{E}_d$.

V. COMBINED PULSED AND CONTINUOUS DISCHARGES

Much of the current research in the development of electric discharge COILs has focused on engineering the operating E/N of the discharge to be closer to the optimal value for
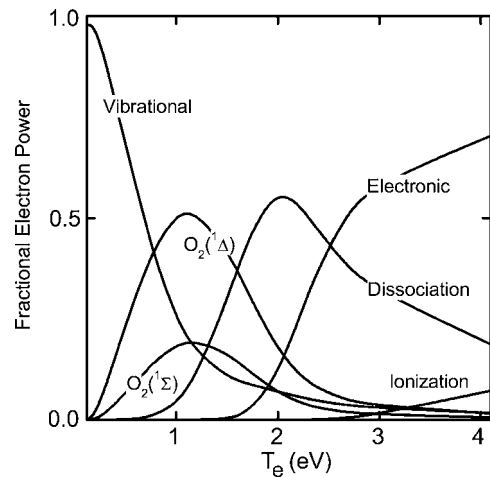

FIG. 8. Fraction of electron power deposited into various processes in pure O_2 as a function of T_e.

$O_2(^1\Delta)$ production. The fractions of electron power dissipated by various electron-impact processes as a function of electron temperature in pure O_2 are shown in Fig. 8(a). To optimize the fraction of power that is directly dissipated in the electron-impact production of $O_2(^1\Delta)$ [Eq. (23)] the electron temperature should be near 1.2 eV, which corresponds to an E/N of ≈ 10 Td (Townsend). Unfortunately, self-sustained discharges in He/O_2 mixtures operate at at least a few tens of Townsend,[22,32] roughly corresponding to the peak in dissociation at T_e=2.1 eV. Various methods have been investigated to manage the E/N, such as increasing the number density of the gas with an inert diluent such as He,[32] adding other components to reduce the ionization potential of the gas such as NO,[33] or by sustaining ionization via an e-beam.[15]

Another method is to use a pulsed discharge akin to that proposed by Hill,[11] wherein a short, high power pulse is applied, followed by a longer period of lower power before applying another high power pulse. The duration of the high power pulse should be long enough for the electron temperature to spike and for the gas to avalanche, producing an electron density in excess of the steady-state value. The high power pulse should be short enough so that the discharge does not comes into a quasi-equilibrium. If there is sufficient excess ionization during the period of lower power deposition, there may be an extended period where T_e falls below the self-sustaining value, which for He/O_2 mixtures enables a more efficient production of $O_2(^1\Delta)$. The length of time the low power pulse is applied is largely determined by the time required for the electron density to decrease to its steady-state value, thereby increasing the impedance of the discharge and increasing T_e. This configuration is often referred to as spiker-sustainer excitation.

These principles are demonstrated using the results from the global kinetics model.[22] A He/O_2=50/50 gas mixture at 5 Torr is excited by a spiker pulse with a duration of 100 ns, followed by a sustainer pulse of 1 W/cm³ for a duration of 1.5 µs. The power, and the resulting electron density and electron temperature T_e are shown in Fig. 9 as a function of time for spiker pulses of up to 16 W/cm³. The spiker pulse
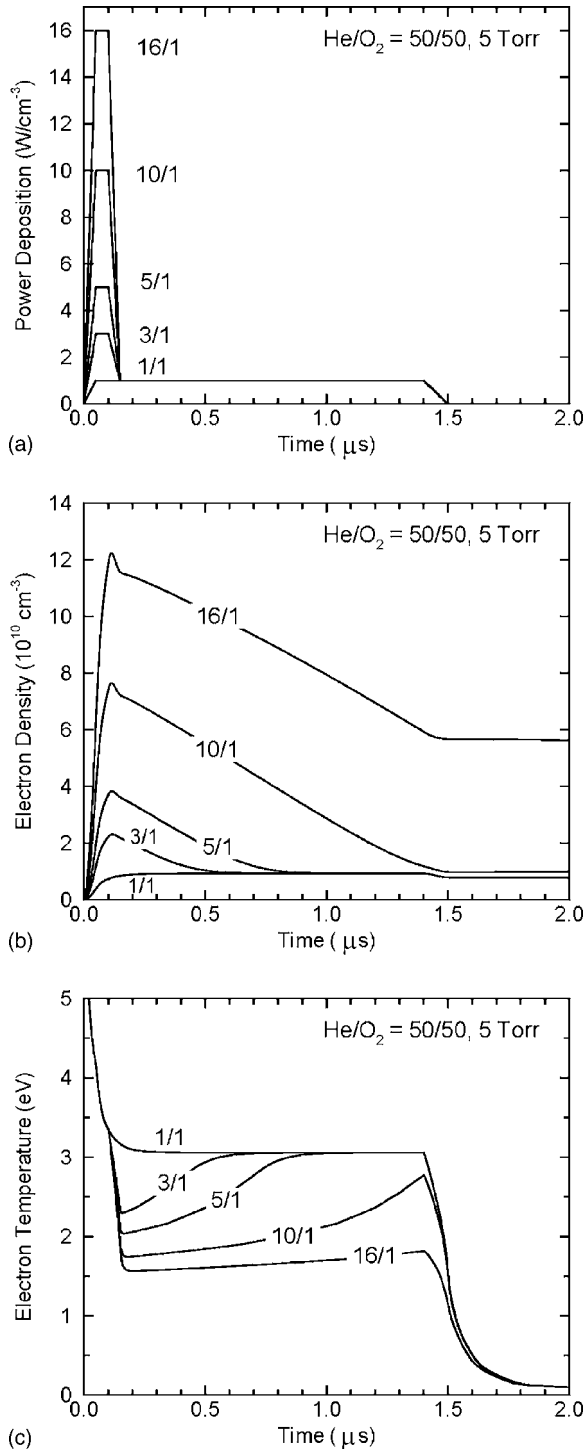
FIG. 9. Plasma properties obtained with the global kinetics model for He/O_2=50/50 mixtures at 5 Torr while varying the spiker power. The fractions indicate the ratio of the spiker power to the sustainer power. (a) Power deposition format, (b) electron density, and (c) electron temperature. The excess electron density produced by the spiker enables the electron temperature to be at a more optimum value for excitation of $O_2(^1\Delta)$.

avalanches the electron density to values as high as 1.2 $\times 10^{11}$ cm^{-3} with 16 W/cm^3. Following the spiker pulse, the electron density begins decaying towards the steady-state electron density for a power of 1 W/cm^3 of n_{eo} $\approx 10^{10}$ cm^{-3}. The quasi-steady-state electron temperature for 1 W/cm^3 is $T_{eo} \approx 3$ eV. As long as the electron density is above n_{eo} then the electron temperature is below T_{eo}. As the

electron density decays to n_{eo}, the electron temperature increases, eventually reaching T_{eo} when the electron density falls to n_{eo}. For spiker powers of up to 10 W/cm^3, the electron density and temperature recover to n_{eo} and T_{eo} during the 1.5 μs duration.

During the time that the electron density is in excess of its quasi-cw value, T_e is below its quasi-cw value, falling to as low as 1.5 eV. This low value is nearly optimum for exciting $O_2(^1\Delta)$ while also minimizing the rate of electron-impact dissociation. The higher power spiker pulses produce larger excesses of ionization which enable T_e to remain below the self-sustaining value for a longer period of time. These lower electron temperatures, coupled with the excess ionization, increase the production of $O_2(^1\Delta)$ significantly above that which would have been obtained depositing the same average power on a cw, self-sustaining basis. This trend is shown in Fig. 10(a) where the yield of $[O_2(^1\Delta)]$ $+[O_2(^1\Sigma)]$ is plotted as a function of the spiker power. The energy efficiency of producing $[O_2(^1\Delta)]+[O_2(^1\Sigma)]$ increases by a factor of nearly 2.5 as the spiker power increases, eventually saturating for a spiker power of 20 W/cm^3. This saturation is simply a consequence of having reached the optimum electron temperature during the sustainer where at best 40% of the power is dissipated in directly exciting $O_2(^1\Delta)$ or $O_2(^1\Sigma)$. The saturation is also in part a result of the depletion of the excess electron density by dissociative attachment.

Note that the electron density decreases rapidly during the sustaining pulse and then decreases less rapidly when the sustainer pulse is terminated and the electron temperature falls to thermal value. These trends result from the electron loss being dominated by dissociative attachment, whose rate coefficient has significant values ($> 5 \times 10^{-12}$ cm^{-3} s^{-1}) for electron temperatures > 1.5 eV. When T_e falls to lower values upon termination of power, the dominant electron-loss mechanism transitions to dissociative recombination or diffusion, both of which have small rates in comparison.

Power deposition, electron density, and T_e are shown in Fig. 11 as a function of the length of the sustainer pulse, from 1 to 2.5 μs. The spiker pulse is 10 W/cm^3 while the sustainer pulse is 1 W/cm^3. Since the power and length of the spiker pulse are fixed, the peak electron density is the same in all cases. T_e decreases to 1.7 eV at the end of the spiker pulse, increasing towards T_{eo} until fully recovering with a sustainer pulse length of 1.75 μs. Pulse lengths longer than this value are essentially self-sustaining as the electron temperature has recovered to T_{eo}. The efficiency of production of $[O_2(^1\Delta)]+[O_2(^1\Sigma)]$ therefore decreases as the length of the sustainer pulse increases, as shown in Fig. 10(b) since the time-averaged electron temperature increases as the length of the sustainer pulse increases. The improvement in efficiency afforded by the spiker-sustainer configuration is essentially lost for sustainer pulse lengths exceeding tens of microseconds. These results provide insights to the optimum interpulse period that elapses prior to applying the next spiker pulse.

The total yield of $[O_2(^1\Delta)]+[O_2(^1\Sigma)]$ as a function of the length of the spiker pulse is shown in Fig. 10(c). The efficiency of excitation decreases as the length of the spiker pulse increases. The ideal situation would be an infinitesi-
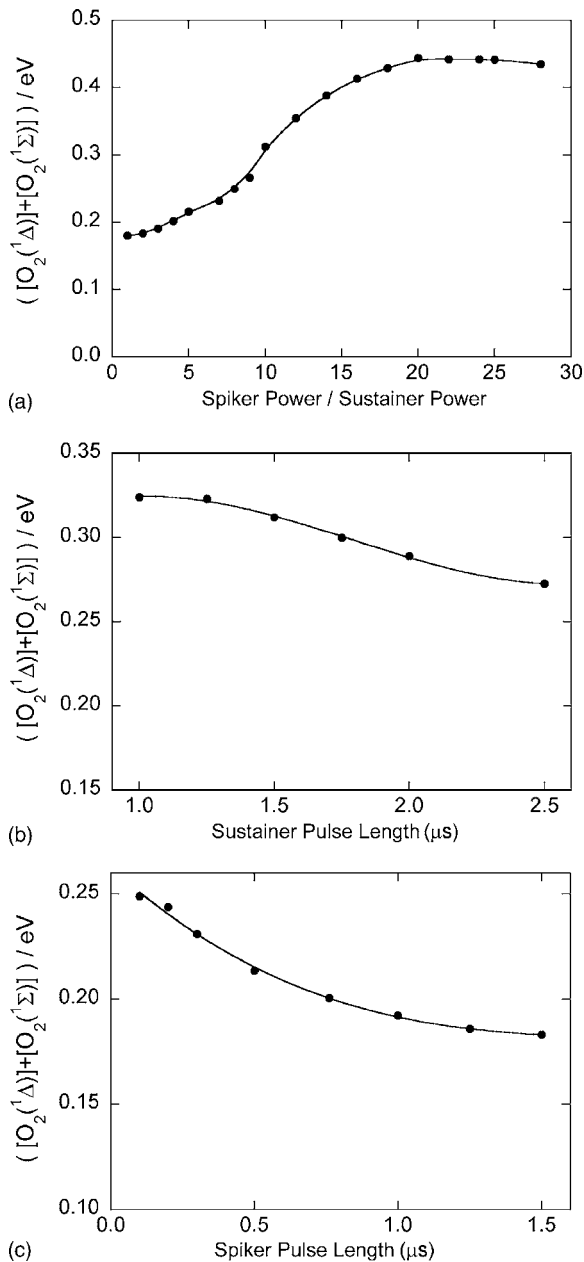
FIG. 10. Efficiency of $O_2(^1\Sigma)$ and $O_2(^1\Delta)$. production obtained with the global kinetics model for spiker-sustainer configurations for He/O_2 =50/50 mixtures at 5 Torr. (a) Efficiency as a function of the ratio of spiker power to sustainer power. (b) Efficiency as a function of the sustainer pulse length. (c) Efficiency as a function of the spiker pulse length.

FIG. 11. Plasma properties obtained with the global kinetics model for He/O_2=50/50 mixtures at 5 Torr while varying the sustainer pulse length. The times indicate the length of the sustainer pulse. (a) Power deposition format, (b) electron density, and (c) electron temperature.

mally short spiker pulse producing an instantaneous excess in electron density. As the length of the spiker pulse increases, the discharge transitions into a self-sustaining mode at the higher power level. Although the total amount of $[O_2(^1\Delta)]+[O_2(^1\Sigma)]$ produced is larger, the efficiency with which this higher production is achieved is lower.

The spiker-sustainer concept was investigated using the 1D model to determine if finite residence time effects of the reactants in the discharge, and extension of the plasma upstream and downstream of the primary discharge zone, would compromise the potential for increasing the efficiency of production of $O_2(^1\Delta)$. A 2.5 kW pulse was applied for 100 ns, followed by 1, 2, and 4 μs sustainer pulses at rep-

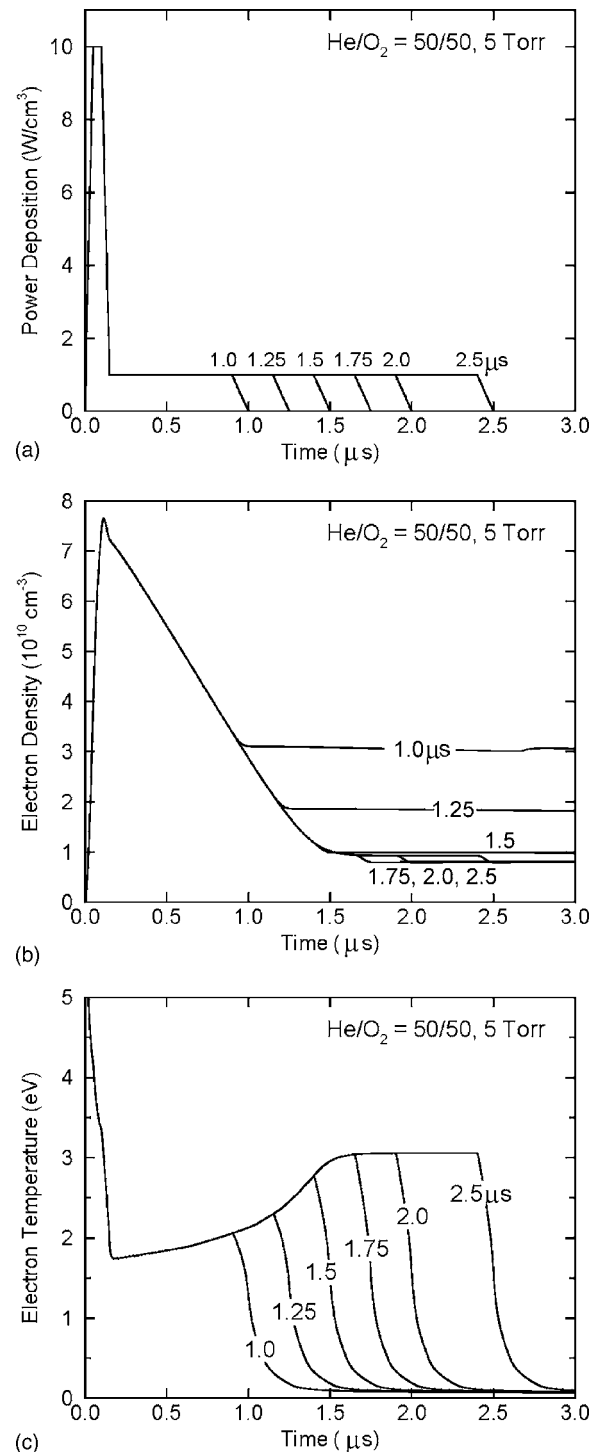etition rates of 1 MHz, 500 kHz, and 250 kHz. The average power was 340 W which, due to the short duration of the spiker pulse, is also approximately the value of power during the sustainer period. A sufficient number of spiker-sustainer periods were simulated in order for the system to come into a pulse-periodic steady state.

The electron temperature is, on a pulsed averaged basis, lower with the spiker sustainer compared to the cw case, as
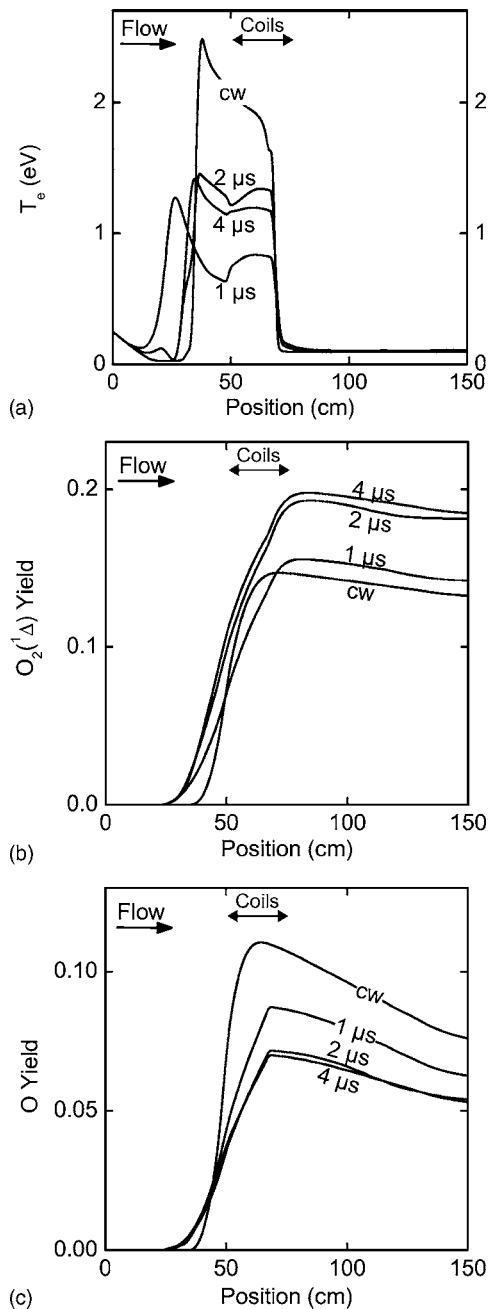
FIG. 12. Plasma properties for 1, 2, and 4 μs interpulse periods compared to a continuous discharge. The average power deposition is 340 W. (a) Electron temperature when the sustainer power is applied. (b) $O_2(^1\Delta)$ yield and (c) O yield along the discharge. The electron temperature decreased from ≈ 2 to ≈ 1 eV for the pulsed cases—a value more favorable for $O_2(^1\Delta)$ production.

shown in Fig. 12(a). The average electron temperature in the cw discharge of ≈ 2 eV corresponds to the peak in electron-impact dissociation of O_2, while the average temperature for the 2 and 4 μs interpulse periods is closer to 1 eV, corresponding to the peak in $O_2(^1\Delta)$ excitation, as shown in Fig. 8. The result is approximately a 50% improvement in $O_2(^1\Delta)$ yield as shown in Fig. 12(b). Although the background electron temperature is lower for the 1 μs interpulse period than for the 2 and 4 μs interpulse periods, the overall fraction of time spent in the high power pulse is twice as long, thereby lowering the $O_2(^1\Delta)$ yield obtained with the 1 μs interpulse

period. The reduced O atom yield shown in Fig. 12(c) confirms that for all three pulse power formats the discharge is no longer operating at an electron temperature that favors O_2 dissociation.

The $O_2(^1\Delta)$ yield produced for these conditions has nearly saturated with the 2 μs interpulse period. Longer interpulse periods do not increase $O_2(^1\Delta)$ yields as confirmed by performing simulations with 10 and 20 μs interpulse periods. The reasoning is similar to that discussed for the results from the global model. For longer interpulse periods, the discharge transitions back into a self-sustaining mode with a higher electron temperature.

The pulsed discharges were the only cases investigated that show significant departures from the specific energy deposition scaling predicted by the global model.[22] At the same $\bar{E}_d$ as the base case (0.88 eV/molecule) the 2 and 4 μs delays produced almost 50% higher $O_2(^1\Delta)$ yields than the base case. With further optimization of the pulse power, duration, delay, and background power, the pulsed schemes might produce even larger yields. Pulsed schemes may also be helpful in alleviating discharge instability problems caused by gas heating and resultant rarefaction and discharge constriction.

VI. CONCLUDING REMARKS

The effects of axial transport and pulsed power formats have been investigated with a global kinetics and one-dimensional axial flowing plasma kinetics models. The one-dimensional results for cw capacitively coupled discharges produced nearly the same scaling of $O_2(^1\Delta)$ yield with specific energy deposition as the previous zero-dimensional model in the somewhat smaller parameter space investigated. The effects caused by adding an inert diluent, increasing the power, and changing the flow velocity were shown to be smaller than the contribution of specific energy deposition, as predicted by the global model. Comparing the global model, which is essentially inductive coupling, with the CCP model in one dimension, showed that CCP discharges promote slightly higher $O_2(^1\Delta)$ yields due to a more optimal (lower) electron temperature in the bulk plasma; however, their energy scales are nearly the same. Pulsed discharges showed the most promise for improving yields. Maximum theoretical yields predicted with the global kinetics model provided up to factors of 2 improvement. With modest pulsing schemes $O_2(^1\Delta)$ yields of 50% higher than the cw cases at the same $\bar{E}_d$ while reducing O_2 dissociation were predicted with the 1D model. Further increases in the optical gain of electric discharge COIL experiments can likely be achieved by practical application of pulsed rf discharges.

[1] W. E. McDermott, N. R. Pchelkin, D. J. Benard, and R. R. Bousek, Appl. Phys. Lett. **32**, 469 (1978).

[2] H. Fujii, S. Yoshida, M. Iizuka, and T. Atsuta, J. Appl. Phys. **67**, 3948 (1990).

[3] A. Elior, B. D. Barmashenko, E. Lebiush, and S. Rosenwaks, Appl. Phys. B: Lasers Opt. **61**, 37 (1995).

[4] M. Endo *et al.*, IEEE J. Quantum Electron. **34**, 393 (1998).

[5] D. Furman, E. Bruins, V. Rybalkin, B. D. Barmashenko, and S. Rosenwaks, IEEE J. Quantum Electron. **37**, 174 (2001).

[6] J. Kodymova, O. Spalek, V. Jirasek, M. Censky, and G. D. Hager, Appl. Phys. A: Mater. Sci. Process. **77**, 331 (2003).

[7] http://www.boeing.com/defense-space/military/abl/flash.html

[8] J. Kodymova and O. Spalek, Jpn. J. Appl. Phys., Part 1 **37**, 117 (1998).

[9] D. L. Carroll and W. C. Solomon, *ElectriCOIL: An Advanced Chemical Iodine Laser Concept*, Proceedings of the XIII International Symposium on Gas Flow and Chemical Lasers and High Power Laser Conference, Florence, Italy, 18–22 September 2000, edited by A. Lapucci (SPIE, Bellingham, WA, 2000), pp. 40–44.

[10] T. L. Henshaw, T. J. Madden, G. C. M. Il, B. T. Anderson, R. F. Tate, M. R. Berman, and G. D. Hager, AIAA Paper No. 2000-2424 (2000).

[11] A. Hill, *The Next Generation of Controlled Avalanche Discharge Gas Lasers*, International Conference on Lasers, Albuquerque, NM, 2000 (STS, McLean, VA, 2000).

[12] A. P. Napartovich, A. Deryugin, and I. Kochetov, J. Phys. D **34**, 1827 (2001).

[13] J. Schmiedberger and H. Fujii, Appl. Phys. Lett. **78**, 2649 (2001).

[14] D. L. Carroll, D. M. King, J. T. Verdeyen, B. Woodard, J. W. Zimmerman, L. Skorski, and W. C. Solomon, AIAA Paper No. 2003-4029 (2003).

[15] A. A. Ionin, Y. M. Klimachev, A. A. Kotkov, I. V. Kochetov, A. P. Napartovich, L. V. Seleznev, D. V. Sinitsyn, and G. D. Hager, J. Phys. D **36**, 982 (2003).

[16] J. F. Hon, D. N. Plummer, P. G. Crowell, J. Erkkila, G. D. Hager, C. A. Helms, and K. A. Truesdell, AIAA Paper No. 94-2422 (1994).

[17] D. J. Benard and N. R. Pchelkin, Rev. Sci. Instrum. **49**, 794 (1978).

[18] G. Fournier, J. Bonnet, D. David, and D. Pigache, *Excitation of Singlet Oxygen at Atmospheric Pressure*, Proceedings of Phenomena in Ionized Gases II, Minsk, 1981, pp. 837–838.

[19] D. L. Carroll, J. T. Verdeyen, D. M. King, B. Woodard, L. Skorski, J. W. Zimmerman, and W. C. Solomon, *Recent Work on the Development of an Electric Discharge Oxygen Iodine Laser*, XIV International Symposium on Gas Flow and Chemical Lasers and High Power Laser Conference, Wroclaw, Poland, 2002, edited by K. Abramski, E. Plinski, and W. Wolinski (SPIE, Bellingham, 2002), pp. 316–326.

[20] T. V. Rakhimova *et al.*, AIAA Paper No. 2003-4306 (2003).

[21] Y. V. Savin *et al.*, AIAA Paper No. 2003-4305 (2003).

[22] D. S. Stafford and M. J. Kushner, J. Appl. Phys. **96**, 2451 (2004).

[23] D. L. Carroll *et al.*, Appl. Phys. Lett. **85**, 1320 (2004).

[24] D. L. Carroll *et al.*, Appl. Phys. Lett. **86**, 111104 (2005).

[25] A. Hicks, S. Norberg, P. Shawcross, W. Lempert, J. W. Rich, and I. Adamovich, *Singlet Oxygen Generation in a High Pressure Non-Self-Sustained Electric Discharge*, 57th Gaseous Electronics Conference, Bunratty, Ireland, 2004.

[26] S. D. Rockwood, Phys. Rev. A **8**, 2348 (1973).

[27] P. N. Brown, G. D. Byrne, and A. C. Hindmarsh, SIAM (Soc. Ind. Appl. Math.) J. Sci. Stat. Comput. **10**, 1038 (1989).

[28] R. Atkinson, D. L. Baulch, R. A. Cox, J. R. F. Hampson, J. A. Kerr, M. J. Rossi, and J. Troe, J. Phys. Chem. Ref. Data **26**, 521 (1997).

[29] S. M. Newman, A. J. Orr-Ewing, D. A. Newnham, and J. Ballard, J. Phys. Chem. A **104**, 9467 (2000).

[30] J. T. Herron and D. S. Green, Plasma Chem. Plasma Process. **21**, 459 (2001).

[31] B. F. Gordiets, C. M. Ferreira, V. L. Guerra, J. Loureiro, J. Nahorny, D. Pagnon, M. Touzeau, and M. Vialle, IEEE Trans. Plasma Sci. **23**, 750 (1995).

[32] J. T. Verdeyen, D. M. King, D. L. Carroll, and W. C. Solomon, *Diagnostic Development for the ElectriCOIL Flow System*, Proceedings of the Gas and Chemical Lasers and Intense Beam Applications III Conference, San Jose, CA, 22–24 January 2002, edited by S. Davis and M. Heaven (SPIE, Bellingham, WA, 2002), pp. 154–160.

[33] D. L. Carroll *et al.*, IEEE J. Quantum Electron. **41**, 213 (2005).